Ferromagnetism of MnxSi1-x(x ~ 0.5) films grown in the shadow geometry by pulsed laser deposition method

S. N. Nikolaev, A. S. Semisalova, V. V. Rylkov, V. V. Tugushev, A. V. Zenkevich, A. L. Vasiliev, E. M. Pashaev, K. Yu. Chernoglazov, Yu. M. Chesnokov, I. A. Likhachev, N. S. Perov, Yu. A. Matveyev, O. A. Novodvorskii, E. T. Kulatov, A. S. Bugaev, Y. Wang, and S. Zhou

Citation: AIP Advances **6**, 015020 (2016); doi: 10.1063/1.4941357
View online: http://dx.doi.org/10.1063/1.4941357
View Table of Contents: http://scitation.aip.org/content/aip/journal/adva/6/1?ver=pdfcov
Published by the AIP Publishing

Ferromagnetism of Mn_xSi_{1-x}(x~0.5) films grown in the shadow geometry by pulsed laser deposition method

S. N. Nikolaev,[1] A. S. Semisalova,[2,3] V. V. Rylkov,[1,4,a] V. V. Tugushev,[1,5,b] A. V. Zenkevich,[6,7] A. L. Vasiliev,[1] E. M. Pashaev,[1] K. Yu. Chernoglazov,[1] Yu. M. Chesnokov,[1] I. A. Likhachev,[1] N. S. Perov,[3] Yu. A. Matveyev,[6,7] O. A. Novodvorskii,[8] E. T. Kulatov,[5] A. S. Bugaev,[4,6] Y. Wang,[2] and S. Zhou[2]

[1]*National Research Centre "Kurchatov Institute", 123182 Moscow, Russia*
[2]*Helmholtz-Zentrum Dresden-Rossendorf, Institute of Ion Beam Physics and Materials Research, Bautzner Landstrasse 400, 01328 Dresden, Germany*
[3]*Faculty of Physics, Lomonosov Moscow State University, 119991 Moscow, Russia*
[4]*Kotel'nikov Institute of Radio Engineering and Electronics RAS, 141190 Fryazino, Moscow Region, Russia*
[5]*Prokhorov General Physics Institute RAS, 119991 Moscow, Russia*
[6]*Moscow Institute of Physics and Technology, 141700 Dolgoprudny, Moscow Region, Russia*
[7]*National Research Nuclear University "MEPhI", 115409 Moscow, Russia*
[8]*Institute on Laser and Information Technologies RAS, 140700 Shatura, Moscow Region, Russia*

(Received 19 September 2015; accepted 21 January 2016; published online 29 January 2016)

The results of a comprehensive study of magnetic, magneto-transport and structural properties of nonstoichiometric Mn_xSi_{1-x} (x≈0.51-0.52) films grown by the Pulsed Laser Deposition (PLD) technique onto Al_2O_3(0001) single crystal substrates at T = 340°C are present. A highlight of used PLD method is the non-conventional ("shadow") geometry with Kr as a scattering gas during the sample growth. It is found that the films exhibit high-temperature (HT) ferromagnetism (FM) with the Curie temperature T_C ~ 370 K accompanied by positive sign anomalous Hall effect (AHE); they also reveal the polycrystalline structure with unusual distribution of grains in size and shape. It is established that HT FM order is originated from the bottom interfacial self-organizing nanocrystalline layer. The upper layer adopted columnar structure with the lateral grain size ≥ 50 nm, possesses low temperature (LT) type of FM order with T_c ≈ 46 K and contributes essentially to the magnetization at T ≤ 50 K. Under these conditions, AHE changes its sign from positive to negative at T ≤ 30K. We attribute observed properties to the synergy of distribution of Mn_xSi_{1-x} crystallites in size and shape as well as peculiarities of defect-induced FM order in shadow geometry grown polycrystalline Mn_xSi_{1-x} (x~0.5) films. [http://dx.doi.org/10.1063/1.4941357]

I. INTRODUCTION

Mn_xSi_{1-x} (x≈0.5) alloyed films with composition close to the manganese monosilicide MnSi are materials with exceptional combination of magnetic and transport properties; at the same time they are promising for spintronic applications.[1–7] The perfect single crystal ε-MnSi with B20-type of structure possesses at low temperatures (≤ 30 K) intriguing magnetic and transport phenomena caused by formation of new magnetic quasiparticles – skyrmions (see Ref. 6 and references therein). On the other hand, the Mn_xSi_{1-x} (x≈0.5) thin layers grown on Si(001) or Al_2O_3(0001) substrates

[a]E-mail: vvrylkov@mail.ru
[b]E-mail: tuvictor@mail.ru

demonstrate the high-temperature (HT) ferromagnetism (FM) with the Curie temperature T_c of the order of room temperature.[2–4] This fact is in contrast to the case of bulk ε-MnSi single crystal, where only the low-temperature (LT) FM was reported with $T_C \approx 30$ K.[8,9] The HT FM order at $x \cong 0.506$ (that just corresponds to the single crystal ε-MnSi belonging to berthollides[9,10]) was observed in the Mn_xSi_{1-x}/Si(001) structures but at enough small Mn_xSi_{1-x} film thickness less than one ε-MnSi monolayer.[2,11] This order is explained by the formation of c-MnSi phase with B2-like (CsCl) crystal structure stabilized with tetragonal distortion due to favorable lattice mismatch between the film and substrate.[1] Recently we reported the HT FM appearance with $T_C \approx 330$ K in 70 nm thick Mn_xSi_{1-x} ($x \approx 0.52$-0.55) films grown on the Al_2O_3(0001) substrates by pulsed laser deposition (PLD) technique.[3,4] We argued that the observed HT FM has a defect-induced nature: it is due to formation of local magnetic moments on the Si vacancies inside the MnSi matrix and the strong exchange coupling between these moments mediated by spin fluctuations of itinerant carriers.[12] The Mn_xSi_{1-x} films in[3,4] were deposited at a relatively slow deposition rate (~2 nm/min) using PLD method in a conventional "direct" geometry (DG) when the surface of Al_2O_3(0001) substrate is exposed to the Mn-Si laser plume. Accordingly to atomic-force microscopy (AFM) measurements, the structure of thus grown films is mosaic, with the crystallite size ~0.5-1 μm.

In this work we present new results of a comprehensive study of structural, magnetic and magneto-transport properties of the Mn_xSi_{1-x} ($x \approx 0.52$) polycrystalline films grown by PLD technique employing unconventional "shadow" geometry (SG) with Kr as a buffer gas.[13] As compared to the conventional "direct" geometry (DG) of Ref. 3 and 4, in the SG method the effective scattering of ablated particles in the buffer gas results in the lower energy of the depositing atoms as well as very high deposition rate.[13] We found that SG grown Mn_xSi_{1-x} ($x \approx 0.5$) films have two magnetic phases: HT FM phase with $T_C \approx 370$ K and LT FM phase with $T_C \approx 46$ K. At the same time, the anomalous Hall effect (AHE) changes its sign from the positive to negative one at the temperature below 30 K. We explain obtained experimental results by the interplay of two effects: 1) self-organization of polycrystalline film leading to the formation of two layers in which the crystallites strongly differ in size and shape; 2) peculiarities of defect-induced FM ordering in such a system.

II. SAMPLES AND EXPERIMENTAL DETAILS

The SG grown Mn_xSi_{1-x} thin films were deposited in Kr atmosphere (~10^{-2} mbar) onto the α-Al_2O_3(0001) substrates 10x15 mm^2 in size using the single crystal MnSi target.[13] The substrate temperature during the deposition (340 °C) was the same as for previous DG deposited films, while the deposition rate was higher (≥ 7 nm/min). The Rutherford backscattering spectrometry (RBS) was used to determine the film composition and thickness.[13] The film thickness d depends on the distance L to the target; the value d decreases from 270 to 70 nm with the increase of L at the length $\delta L \approx 15$ mm. The Mn content at the same deposited area increases from 0.506 up to 0.517. The Mn content at the same deposited area increases from 0.506 up to 0.517, but most strongly the Mn content and film thickness change at the substrate edge located closer to the target.[13] When the film thickness decreases from 160 to 70 nm ($\delta L \approx 10$ mm), the film composition slightly changes with L ($x \approx 0.514$-0.517). To investigate the effect of the film composition and deposition rate on the structural, magnetic and magneto-transport properties, the as grown sample was cut into seven 2x10 mm^2 stripes with different thicknesses.

The structural properties of Mn_xSi_{1-x}/α-Al_2O_3 samples were investigated by X-ray diffraction (XRD) measurements using a Rigaku SmartLab diffractometer. To elucidate the microscopic structure of Mn-Si films, they were further investigated by scanning transmission electron microscopy (STEM) using TITAN 80-300 TEM/STEM instrument (FEI, US) operating at an accelerating voltage of U=300 kV, equipped with Cs-probe corrector, high-angle annular dark-field detector (HAADF) (Fischione, US) and energy dispersive X-ray (EDX) microanalysis spectrometer (EDAX, US). The Mn_xSi_{1-x}/α-Al_2O_3 samples with the film thickness of 250 nm ($x \approx 0.51$) and 100 nm ($x \approx 0.516$) were studied. The cross-sections of the films were prepared by the mechanical polishing of sandwiched pieces followed by Ar^+ ion-beam milling until perforation in Gatan PIPS (Gatan, US).

The temperature dependences of saturation magnetization and the magnetic hysteresis of the SG grown Mn_xSi_{1-x} films 2x1.5 mm^2 in size were measured by superconducting quantum interference device MPMS-3 (SQUID-VSM) magnetometer between 5 and 400 K at in plane magnetic fields $\mu_0 H$ till 1.5 T. The uncertainty in measurements of coercivity was about 5 Oe.

The Hall effect and conductivity were studied in the 2x8 mm^2 stripes of Mn_xSi_{1-x} films in the double Hall bar geometry. Contacts were fabricated by the soldering indium with the distance between potential probes $l \approx 2.5$ mm. Details of Hall effect measurements were described in Refs. 3 and 4. We used the same procedure and measured lateral resistance R_{xy} at various polarities of magnetic field B at the "downward" and "upward" scanning directions of B; then expanded obtained function $R_{xy}(B)$ in odd and even components. Such an approach makes it possible to extract Hall component from $R_{xy}(B)$ with possible hysteresis in the behavior of the Hall resistance R_H and to suppress the parasitic contribution of the magnetoresistance to R_{xy} as well as to distinguish possible even contributions of the incoherent mesoscopic effect or the planar Hall effect (for details see Refs. 14 and 15).

III. STRUCTURE MEASUREMENTS

The results of XRD measurements of as grown $Mn_xSi_{1-x}/Al_2O_3(0001)$ samples 10x15 mm^2 in size (before cutting) are shown in Fig. 1. The angular range 2θ = 30-70° contains several peaks, which are all attributed to ε-MnSi phase with B20 structure. An additional intense diffraction peak observed at 2θ = 64.5° does not belong to ε-MnSi and could point at (200) plane diffraction of c-MnSi phase (similarly to c-FeSi phase in Ref. 16). However, further analysis of XRD rocking curve reveals that this peak originated from a quasi-forbidden reflection (0009) of Al_2O_3 substrate and appears as a result of multiple reflections (so-called multi-wave diffraction, see insert to Fig. 1).

The structural perfection of the film is described by such an integral characteristic as the FWHM of the peak in the rocking curve (FWHMω). FWHMω value for the single-crystalline films should lie in the range between 64 seconds of arc and 245 seconds of arc for the samples under the study with layer thicknesses between 70 nm and 270 nm. At the same time at fig. 1 FWHMω parameter at 2θ = 44,43° is approximately 550 seconds of arc. Such a broad peak is a signature of a pronounced mosaicity of the film structure as well as of a presence of structural defects in PLD grown ε-MnSi films.

The low magnification bright field (BF) TEM image of Mn_xSi_{1-x}/α-Al_2O_3 with the film thickness of $d \approx 250$ nm is presented in Fig. 2(a). The Mn_xSi_{1-x} film exhibited columnar microstructure with the lateral grain sizes of about 50 nm. The electron diffraction (not shown here) and Fourier analysis of High Resolution (HR) TEM images (Fig. 2(b) and the insert) unambiguously

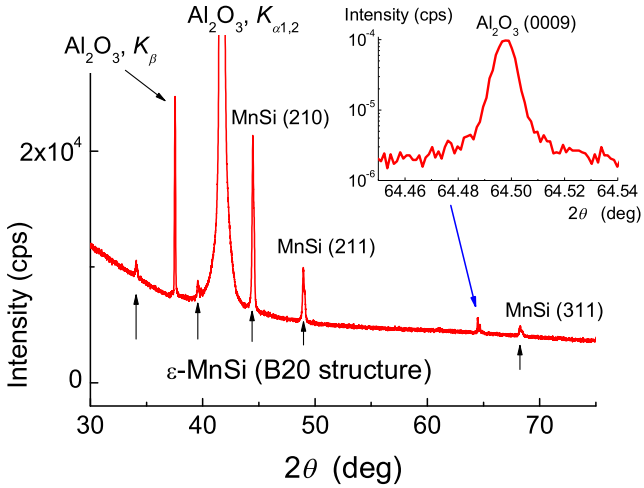

FIG. 1. The results of X-ray diffractometry for SG $Si_{1-x}Mn_x/Al_2O_3(0001)$ structure. Insert shows quasi-forbidden reflection (0009) from Al_2O_3 substrate.

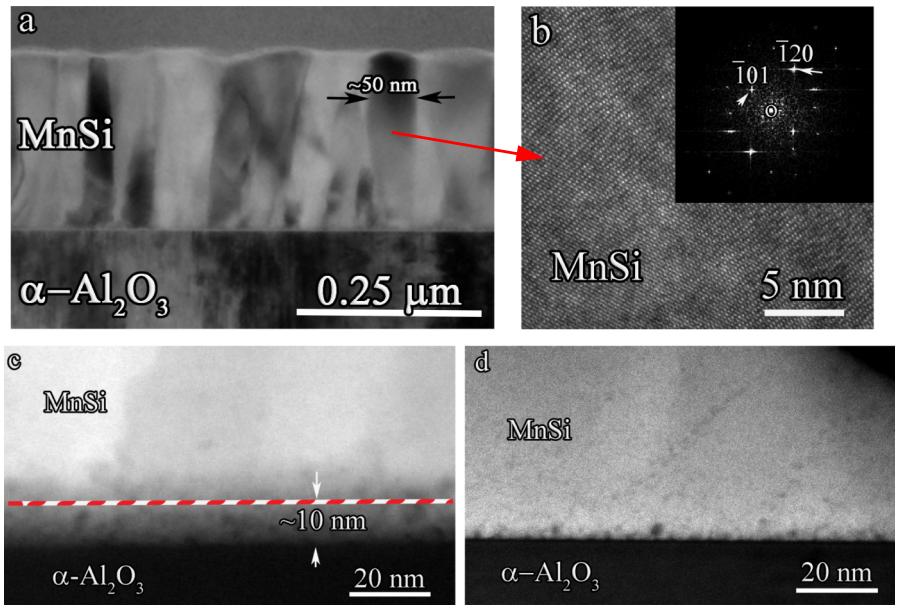

FIG. 2. (a) Low magnification cross-section bright field TEM image of 250 nm SG grown $Si_{1-x}Mn_x/Al_2O_3(0001)$ sample. Note the columnar structure of the top layer mean lateral grain size of 50 nm. (b) The HR TEM image of the columnar grain with FFT spectra in the inset. The FFT spectra indicated that the $Si_{1-x}Mn_x$ grain adopted B20 crystal structure observed in [212] zone axis. The HR TEM image was obtained from the middle part of the grain. (c) The enlarged HAADF STEM image of the interface area of the 250 nm SG grown $Si_{1-x}Mn_x/Al_2O_3(0001)$ sample. The 10 nm layer at the interface have the contrast differs from the upper part of the film. (d) The interface area of the 100 nm SG grown $Si_{1-x}Mn_x/Al_2O_3(0001)$ sample.

demonstrated that the grains in the upper Mn_xSi_{1-x} layer adopted the B20 crystal structure type and that is consistent with the XRD data. The HAADF STEM images of the Mn_xSi_{1-x}/α-Al_2O_3 interfaces of the samples with $d \approx 250$ and 100 nm, are presented in Fig 2(c) and Fig. 2(d), correspondingly. These images revealed the presence of thin layer in the Mn_xSi_{1-x} film adjacent to the interface with different morphology: the Mn_xSi_{1-x} particles adopted equi-axed or dome shape with the size of 4-10 nm. The thickness of that layer was of 10 nm. The formation of the layer could be caused by different crystal structure and large crystal lattice mismatch. The Mn_xSi_{1-x} crystal lattice is characterized by cubic B20 structure type (Space group $P2_13$ #198 ["International tables for crystallography" Volume A: Space-Group Symmetry Editor T. Hahn Springer Fifth Edition 2002] with the lattice constant $a \approx 4.56$ Å. Sapphire (α-Al_2O_3) belongs to the space group $R\bar{3}$ c and although being rhombohedral, it is commonly described in terms of hexagonal Miller-Bravais indices with lattice constants $a = 4.7589$ Å, $c = 12.991$ Å. The orientation of α-Al_2O_3 substrate was [0001], which is sixfold and in the sake of the symmetry it could be proposed the growth of cubic Mn_xSi_{1-x} film in [111] direction. In that case the mismatch between $\{1120\}_{\alpha\text{-Al2O3}}$ with $d = 2.38$ Å and $\{111\}_{MnSi}$ with $d = 2.63$ Å is close to 10%, which is huge. The lattice mismatch released through the growth of small grains at the interface in different orientation and these grains form a layer with the thickness of about 10 nm.

The typical HR TEM image of the 100 nm SG grown $Si_{1-x}Mn_x/Al_2O_3(0001)$ sample is shown in Fig. 3. The close inspection of the HR TEM images of the interface area (Fig. 3(a)) with small grains and analysis of Fast Fourier Transform (Fig. 3(b)-3(d)) indicated that these grains adopted B20 crystal structure, similar to the upper layer. The interface between the bottom and upper layer of the Mn_xSi_{1-x} film is uneven and blurred, but could be revealed better by HAADF STEM imaging (Fig. 2(c) and 2(d)).

Note also that diluted Mn_xSi_{1-x} ($x < 0.04$) alloys containing Mn-rich nanocolumns were grown by molecular beam epitaxy (MBE) technique in.[17,18] No essential manifestations of HT FM caused by these nanocolumns were revealed in Refs. 17 and 18. I.e. the situation in this case is opposite to Ge-Mn alloys with nanocolumns structure where above room temperature FM was observed.[19]

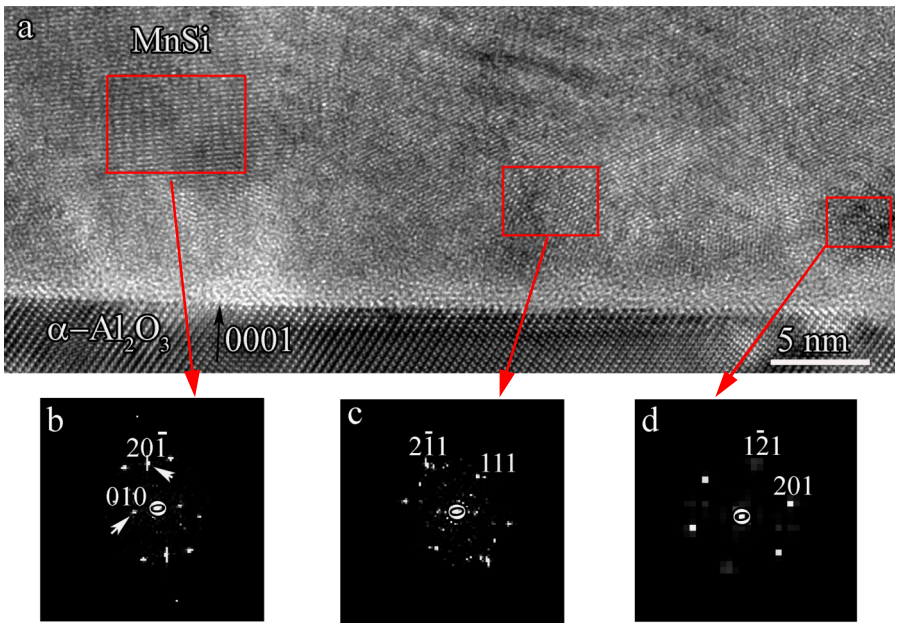

FIG. 3. (a) HR TEM image of the 100 nm SG grown $Si_{1-x}Mn_x/Al_2O_3(0001)$ sample. (b)-(d) FFT spectra from the $Si_{1-x}Mn_x$ grains in [102], [21$\bar{3}$] and [21$\bar{4}$] zone axis, correspondingly.

IV. MAGNETIC AND MAGNETO-TRANSPORT MEASUREMENTS

The temperature dependence of saturation magnetization $M_s(T)$ of three Mn_xSi_{1-x} samples 1-3 ($x \approx 0.517$, 0.516 and 0.514) with the thicknesses $d \approx 70$, 90 and 160 nm, respectively, is presented in Fig. 4. The applied field was $\mu_0 H = 1$ T. The obtained data of Fig. 4 revealed a presence of two ferromagnetic phases: a HT phase with $T_C \approx 370$ K and a LT phase with $T_C \approx 46$ K. The relative contribution of the LT FM phase clearly increases with the increase of the film thickness. Such behavior is in contrast to that of DG grown Mn_xSi_{1-x} films (Fig. 5). When $x \approx 0.52$, the decrease of $M_s(T)$ in the temperature range T = 10-100 K does not exceed 6% and fits well to the Bloch law.[13]

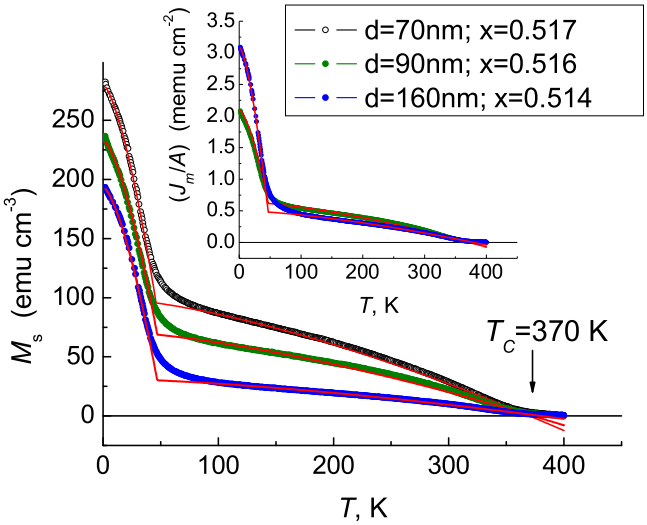

FIG. 4. Temperature dependence of saturation magnetization M_s for Mn_xSi_{1-x} films with different thickness and close Mn content ($x \approx 0.516$) grown in shadow geometry. The insert shows the temperature dependence of magnetic moment J_m normalized by film square A. (For sample with $d = 70$ nm the $J_m(T)/A$ curve practically coincides with one for sample with $d = 90$ nm and is not shown on the insert). Solid lines are fitting dependencies of $M_s(T)$ with using equation (2).

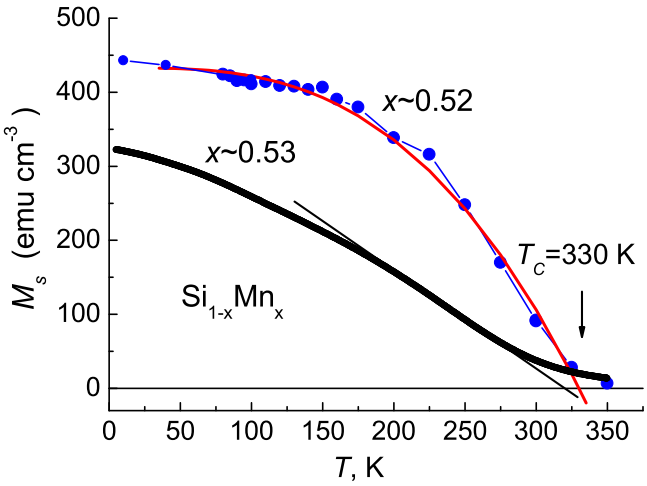

FIG. 5. Temperature dependence of saturation magnetization M_s for Mn_xSi_{1-x} films with $x \approx 0.52$ and 0.53 ($d \approx 70$ nm) grown at "direct" geometry by PLD. Solid line is calculated dependence of $M_s(T)$ from Ref. 3.

Moreover, the $M_s(T)$ value does not increase significantly with lowering T even in case of HT FM degradation, as observed in DG films with the Mn content $x \geq 0.53$ (Fig. 5, see also Ref. 3).

Fig. 6 shows the magnetization vs. magnetic field $M(H)$ dependence for the sample 1 ($x \approx 0.517$, d $\approx$ 70 nm) at T = 5, 100 and 300 K. The open hysteresis loops are clearly visible at temperature below 100 K (see right inset), which is not observed in bulk ε-MnSi single crystal. Left inset in Fig. 5 shows the temperature dependence of coercivity - even at room temperature the coercivity is about 20 Oe. The magnetization saturates in the magnetic field $\mu_0 H \approx 0.6\,T$ at low temperature ($T = 5\ K$) and then linearly increases like in the case of ε-MnSi single crystal.[9,20] At room temperature the saturation field value decreases till $\mu_0 H \approx 0.2$ T.

It is curiously to note that at $T > 46$ K the "surface density" of magnetic moment J_m/A of the HT FM phase (i.e. the total magnetic moment J_m normalized to the film surface A; see inset to Fig. 1) does not depend practically on the film thickness. This fact clearly indicates that the HT FM phase ($T_{Ch} \approx 370$ K) is formed mainly in the interfacial layer directly grown on the substrate with a fixed effective thickness d_1, while the LT FM phase ($T_{Cl} \approx 46$ K) is formed in the upper layer with a variable thickness $d_2 = (d - d_1)$. So, the magnetometry data allude to a presence of two

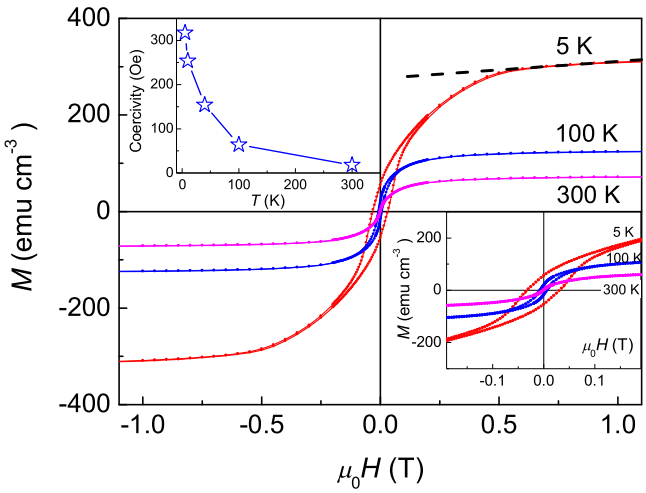

FIG. 6. Magnetization versus magnetic field for SG grown sample 1 ($d \approx 70$ nm; $x \approx 0.517$) at different temperatures. The left inset shows the temperature dependence of coercivity, the right inset shows the enlarged view of central part of $M(H)$ dependences.

FM layers with different effective thicknesses, magnetic moments and Curie temperatures in our films. Hereinafter we will imply the value of $d_1 = J_m/A \cdot M_{sh}$ as an effective thickness, where M_{sh} is the saturation magnetization of HT phase. In our case it means that $d_1 \approx$ const when $M_{sh} \approx$ const. We will also use the term "two-layer system" only as a quite symbolic, to emphasize the relative dominance of columnar microstructure of the B20 phase in the LT upper layer of Si-Mn film. Obviously, partial penetration of this phase into the HT interfacial layer is possible, leading to an absence of clear geometrical boundary between two layers.

The Hall effect provides rich information on the correlation between magnetic and transport properties of Mn-Si system under investigation. Let us recall that in "ordinary" FM material, the Hall resistance R_H contains two components following the expression[21]:

$$R_H d = \rho_H = \rho_H^n + \rho_H^a, \quad \rho_H^n = R_0 B, \quad \rho_H^a = R_s M, \tag{1}$$

where ρ_H is the total Hall resistivity, ρ_H^n and ρ_H^a are the normal and anomalous components of the Hall resistivity, respectively, d is the thickness of FM material, R_0 is the normal Hall effect constant related to the Lorentz force, B is magnetic induction, $R_s \propto (\rho_{xx})^\alpha$ is the anomalous Hall effect (AHE) constant related to the spin-orbit interaction in FM material, M is the magnetization. For a "skew-scattering" driven mechanism of AHE, $\alpha = 1$, and for "intrinsic" and "side-jump" mechanisms of AHE, index $\alpha = 2$.[21] Usually, at the temperature $T \leq T_C$ and for the magnetic field corresponding to the saturation magnetization, the second term in Eq.(1) dominates, i.e. $\rho_H^n << \rho_H^a$. Note that in the case of ε-MnSi single crystal, the third term may also appear in Eq.(1) due to skyrmions formation[22] (so-called component of the topological Hall effect), but in our system we presume that skyrmions are destroyed due to the scattering on the structural and magnetic disorder in the Mn_xSi_{1-x} alloy.

Fig. 7 demonstrates the magnetic field dependence of $\rho_H(B)$, as measured for the sample 1 ($d \approx 70$ nm, $x \approx 0.517$) at the temperature range T = 5-160 K. One can see that the anomalous component ρ_H^a in the saturation regime (at $B \geq 1$ T) decreases up to 10 times as the temperature decreases from 160 K to 5 K. One can notice that in case of the DG grown film the value of ρ_H^a in the same temperature range is either nearly constant (for $x \approx 0.52$) or increases as the temperature

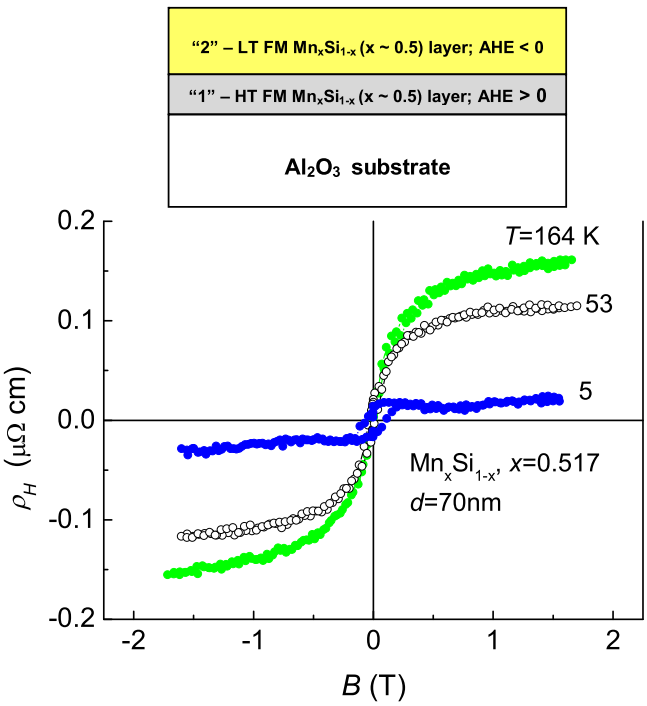

FIG. 7. Resistivity of the Hall effect versus magnetic field for SG grown sample 1 ($d \approx 70$ nm; $x \approx 0.517$) at different temperatures. The inset shows the schematic drawing of Mn_xSi_{1-x}/Al_2O_3 structure.

lowers (up to 2 times for $x \approx 0.55$, see Fig. 4(a) from Ref. 3). The unusual behavior of $\rho_H(B)$ in the SG grown film can be explained in the frame of effective "two-layer system", i.e. as a partial compensation of the positive Hall emf from the bottom HT FM layer and the negative Hall emf from the upper LT FM layer (see inset to Fig. 7). To justify this explanation we have to suggest that in the upper layer, the effect of LT FM order on the Hall transport is similar to the case of bulk ε-MnSi, where AHE has the negative sign.[20,22] At the same time, we have to postulate that in the interfacial layer, the effect of the HT FM order on the Hall transport is similar to the case of DG films,[3] where the AHE of positive sign was reported[3] (the AHE of positive sign is observed also in amorphous Mn_xSi_{1-x} alloys.[7,23]) Evidently, in the two-layer SG grown film a partial compensation of negative and positive contributions $\rho_H(B)$ should be more pronounced at temperatures below the Curie temperature of the LT FM layer ($T_{Cl} \approx 46$ K); this compensation becomes more efficient with the film thickness increasing.

The temperature dependence of $\rho_H(T)$ of the thicker sample 2 ($d \approx 90$ nm, $x \approx 0.516$) measured at $B = 1.2$ T is presented in Fig. 8(a). One can see that below $T \approx 50$ K the $\rho_H(T)$ function falls down and then changes its sign to the opposite below $T \approx 30$ K. At $T = 40$ K a small observed hysteresis of $\rho_H(B)$ curve has the normal form like for sample 1 at $T = 5$ K (see inset in Fig. 8). On the other hand at the temperatures $T \leq 10$ K, the hysteresis loop $\rho_H(B)$ acquires unusual shape (Fig. 8(b)).

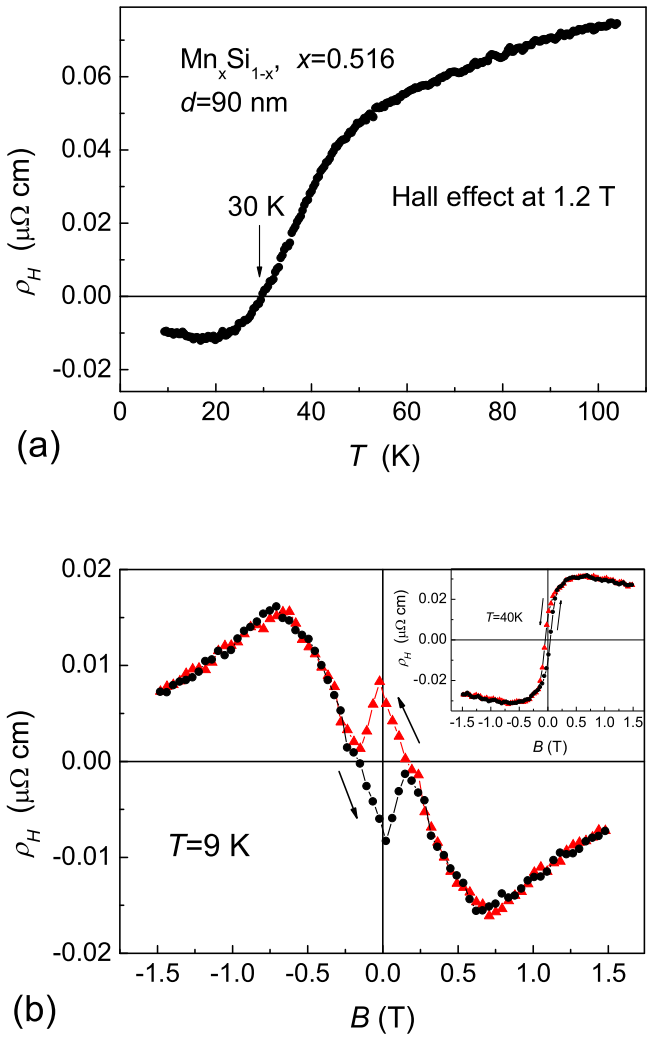

FIG. 8. (a) Temperature dependence of the Hall resistivity for SG grown sample 2 ($d \approx 90$ nm; $x \approx 0.516$) measured at $B = 1.2$ T. (b) Resistivity of the Hall effect $\rho_H(B)$ versus magnetic field for sample 2 at $T = 9$ K. The inset demonstrates $\rho_H(B)$ dependence at $T = 40$ K. Arrows show the "upward" and "downward" scanning directions of B.

Obviously, this is the result of superposition of two AHE components: the first one is hysteretic and provided by HT FM layer, $\rho^a_{H1} > 0$, while the second one is non-hysteretic and provided by the LT FM layer, $\rho^a_{H2} < 0$. Notice, that due to the larger values of thickness and conductivity of the LT FM layer, its contribution to the Hall resistance can be larger in absolute value than that from the HT FM layer (see Eq. (4) below). For both samples with $d \approx 70$ and 90 nm the absolute value of Hall resistivity drop is about 10 times at temperature lowering from ~100 to 10 K. Therefore the crossover from the positive AHE to negative one at low temperatures (~10 K) comes in our case at a critical film thickness of about 80 nm.

The positive sign of ρ^a_{H1} component is not surprising and testifies to a similarity of structural, magnetic and transport properties of the interfacial HT FM layer and DG grown Mn_xSi_{1-x} films. The negative sign of ρ^a_{H2} may be attributed to a similarity of the properties of the upper LT FM layer and ε-MnSi, where ρ^a_H is negative.[20,22] It is also important to note that normal Hall effect in ε-MnSi is positive;[20,22] therefore, the linear behavior of the $\rho_H(B)$ dependence in fields the $B \geq 0.7$ T corresponds to the hole type of conductivity (see Fig. 8(b)).

In addition, introduced two-layer model is confirmed by results of Hall effect investigations in the thick sample 3 ($d \approx 160$ nm, $x \approx 0.514$). In this case it is necessary to expect the dominating contribution to Hall effect from the upper LT layer at low temperatures $T < T_{Cl} \approx 46$ K. It is really observed (see Fig. 9). At $T = 23$ and 10 K AHE is the negative and does not contain the hysteresis in field behavior; the ρ^a_H value falls on absolute value with temperature lowering reaching value of the order of 10^{-2} μΩ·cm as in case of ε-MnSi[20] (in case of ε-MnSi the $|\rho^a_H|$ value is twice smaller). However, at temperatures above Curie temperature $T_{Cl} \approx 46$ K the transition to the positive AHE is observed. At $T = 54$ K the value of ρ^a_H is positive and very small, less than 10^{-2} μΩ·cm (Fig. 9). The observation of positive AHE means that the HT phase in interfacial layer is continuous and forms the infinite cluster.[14]

In order to analyze better the results of Hall effect measurements in the "two-layer system", we have also studied the temperature dependence of longitudinal resistance $R(T)$ for grown SG films. In Fig. 10, the normalized temperature dependences $R(T) = R_{SG}(T)$ and $R(T) = R_{DG}(T)$ (taken from[3]) are shown, respectively, for DG ($d \approx 70$ nm; $x \sim 0.52$) and SG ($d \approx 70$ and 160 nm; $x \sim 0.52$) grown Mn_xSi_{1-x} films, in comparison with $R(T) = R_{SC}(T)$ for ε-MnSi single crystal (taken from[24]). From the data presented in Fig. 10 it follows that resistance $R(T)$ drops more strongly with temperature decreasing than the thick SG grown film: $f(11.5\text{K}) = R(11.5\text{K})/R(290\text{K}) \approx 0.29$ and 0.21 (corresponds $R \approx 6.03$ and 2.15 Ω at 11.5K) for samples with $d \approx 70$ and $d \approx 160$ nm, respectively. (Note that in our case the resistance reaches of approximately residual value at $T \leq 12$ K). The resistance decreasing for perfect epitaxial ε-MnSi films is much stronger and

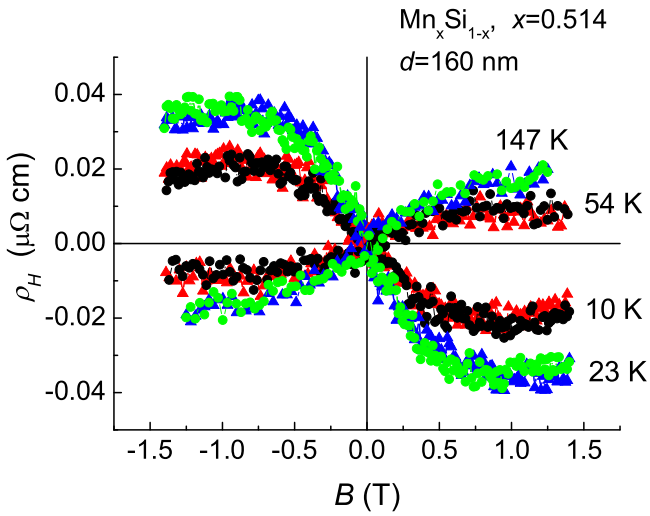

FIG. 9. Resistivity of the Hall effect $\rho_H(B)$ versus magnetic field for SG grown sample 1 ($d \approx 160$ nm; $x \approx 0.514$) at different temperatures. Circles and triangles of curves $\rho_H(B)$ correspond to the "upward" and "downward" scanning directions of B.

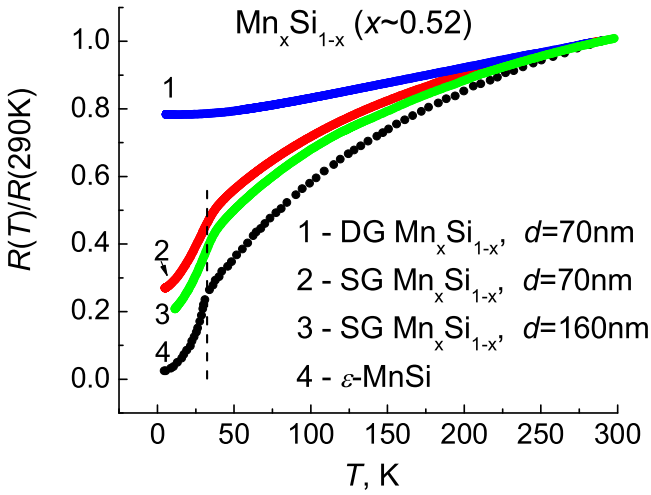

FIG. 10. Normalized temperature dependence of the longitudinal resistance $R(T)$ for DG ($d \approx 70$ nm, curve 1) and SG grown Mn_xSi_{1-x} films ($x \sim 0.52$) with $d \approx 70$ nm (curve 2) and 160 nm (curves 3) in comparison with $\rho(T)$ for $\varepsilon-$MnSi (taken from Ref. 24).

reaches $f \approx 0.03$.[6] Nevertheless, the attention should be paid to the similarity between $R_{SG}(T)$ and $R_{SC}(T)$ and its drastic difference from $R_{DG}(T)$ (Fig. 9).

V. DISCUSSION

The results of TEM investigation unambiguously demonstrated the two-layer structure of Mn_xSi_{1-x} ($x \approx 0.51$-052) films, apparently due to the peculiarity of the SG growth process as well as sufficiently large mismatch (≈ 10%) between the α-Al_2O_3 substrate and Mn_xSi_{1-x} ($x \approx 0.5$) film with B20 structure. The important difference between two layers is the morphology, namely the grain sizes and grain shape. The bottom interfacial HT FM layer, which was deposited directly on the substrate surface is composed of randomly oriented equi-axed or dome shape grains with the average size of 5 nm. The thickness of the layer is about 10 nm. The grains in the upper layer adopted columnar morphology with the diameter of 60-150 nm and propagated to the film surface. Generally, the microstructure of the thick (250 nm) and thin films (100 nm) are similar: bottom Mn_xSi_{1-x} layer adjacent to the interface and top layer. Below we propose the consideration of the magnetic and transport properties of Mn_xSi_{1-x} films ($x \approx 0.51$-0.52) based on that two-layer film morphology or "two-layer system" approximation (see above).

First of all, we have to estimate the value of effective magnetic moment on Mn atom in both layers, suggesting that the density of Mn_xSi_{1-x} ($x \approx 0.51$-0.52) alloy is equal to that of the bulk ε-MnSi single crystal, i.e. ≈ 5.82 g/cm^3.[25] The HT FM and LT FM phase contributions to the total magnetization of the film can be found using the simplified Brillouin function fit for $M_s(T)$:

$$M_s(T) = M_s(0)[1 - (T/T_C)^n]. \quad (2)$$

In our case, $n = 1.5$ leads to the best fit of experimental $M_s(T)$ data (Fig. 1). Using Eq. (2), we have found for the samples with $x \approx$ (0.51-0.52) the effective magnetic moments $m =$ (1.3-1.75) μ_B/Mn and (0.43-0.52) μ_B/Mn for for HT and LT FM phase, respectively (magnetic moments demonstrate a little increase with decreasing the film thickness).

The effective magnetic moment of the interfacial HT FM layer in Mn_xSi_{1-x} films ($x \approx 0.51$-0.52) grown in the SG significantly exceeds the magnetic moment of MnSi single crystal, $m \approx 0.4\ \mu_B$/Mn.[9] It is also higher as compared to the case Mn_xSi_{1-x} film grown in DG ($x \approx 0.52$, $T_C \approx 330$K), where the effective magnetic moment is $m \approx 1.1\ \mu_B$/Mn.[3] These facts do not leave doubt about existence of defect-induced local magnetic moments in the HT FM phase, which are formed due to the same mechanism as in DG grown nonstoichiometric Mn_xSi_{1-x} ($x \approx 0.52$) alloys. The origin of this mechanism, following Ref. 3, consists in the variation of coordination number of Mn atom near the Si

vacancy. Due to a strong hybridization between 3d-electron states of Mn and 3(s,p)-electron states of Si this variation leads to the corresponding local redistribution of charge and spin densities near the Si vacancy, which is thereby responsible for the formation of a complex defect with local magnetic moment ~ (2.0-3.5)μ_B/Mn and effective (average) magnetic moment ~ (1.2-1.75)μ_B/Mn.

The effective magnetic moment of the upper LT FM layer is in good agreement with the magnetic moment of single crystalline ε-MnSi; this fact may be naturally interpreted as an absence of local magnetic moments in the upper LT FM layer. At first glance, this conclusion is surprising, since according to the results of TEM studies and Rutherford backscattering analysis[13] the composition of the film is homogeneous across the film thickness, i.e. LT FM phase contains the same excess amount of Mn atoms as in HT FM phase. Therefore, we have to suggest that most part of Mn containing defects in the upper LT FM layer is in a weak-magnetic or non-magnetic ("magnetically dead") configuration. Following Ref. 3 and 4, as an example of such the configuration we can imagine an interstitial Mn atom introduced into the MnSi matrix. The calculated magnetic moment on this Mn atom is extremely small (~ 0.09μ_B/Mn) and the effective (average) magnetic moment is ~ 0.34μ_B/Mn for Mn_xSi_{1-x} ($x \approx 0.52$) film.

To explain magnetic data we suppose that due to the specificity of the SG method the Si vacancies mainly arise in the interfacial layer of the film. The nanocrystallite boundaries in this layer form a vast network; they eventually can work as the gettering regions for Si vacancies and, consequently, for local magnetic moments on these vacancies. So, following our supposal, nanocrystallite boundaries play the key role in the magnetic properties of HT FM layer, acting as a magnetic envelope of the nanometer scale non-magnetic crystallite. Early in Ref. 12 in the frame of the spin-fluctuation model of FM ordering, we have analyzed the role of dimension effects in granular dilute Si-Mn alloys. We considered the precipitate nanoparticles of $MnSi_{1.7}$ type in the Si matrix and estimated variation of the Curie temperature as a function of the shape and size of these precipitates. Similar analysis can be effectuated for the case of Mn_xSi_{1-x} ($x \sim 0.5$) alloys. For a spherical crystallite of weak itinerant FM with the small radius $r_0 << \zeta$, where ζ is FM correlation length, encircled by an envelope with defect–induced local magnetic moments S having the surface density $\sigma_0 << a^{-2}$, where a is the lattice parameter, we can roughly estimate the Curie temperature T_C as

$$k_B T_C \sim JS(W/v_F Q_{SF})^{1/2}(a/r_0)^{1/2}(\sigma_0 a^2)^{1/2}. \quad (3)$$

Here J is exchange interaction potential between the local moment on the defect and itinerant electron spin, W is itinerant electron bandwidth, v_F is the Fermi velocity, Q_{SF} is spin-fluctuation cutoff wave vector. At $JS \sim 0.1$ eV, $W/v_F Q_{SF} \sim 10$, $a/r_0 \sim 10^{-1}$, $\sigma_0 a^2 \sim 10^{-1} \div 10^{-2}$ we have $T_C \sim 100 \div 400$ K that is not far from above obtained experimental results.

Finally, note that the shape of Mn-rich precipitates can also play a crucial role in the formation of HT FM order. For example, the influence of isovalent Pb surfactant on the growing process of dilute Si-Mn thin films prepared by MBE has been investigated in Ref. 18. It was found that Pb surfactant initiates the formation of nanorod-type ferromagnetic precipitates that lie in the film plane and have T_C above room temperature, while the growing without Pb surfactant creates paramagnetic nanocolumns.

Let us now consider the transport data. As the temperature decreases from 300 to 5 K, the $R_{DG}(T)$ curve in Fig. 10 demonstrates a relatively slow (about 1.3 times) temperature decreasing. It was also shown in Ref. 3 that, contrary to the case of ε-MnSi single crystal, for the DG films the carrier mobility strongly increases (about fifteen times at 60 K), but the carrier concentration drastically decreases (about twenty five times at 100 K). Thus, $R_{DG}(T)$ behavior is driven by an interplay of these two effects and as a result, the value $R_{DG}(T)$ for Mn_xSi_{1-x} ($x \approx 0.52$) film below ~ 40 K significantly exceeds $R_{SC}(T)$ for ε-MnSi, where $R_{SC}(T)$ falls down dramatically.[24]

The physical origin of this remarkable phenomenon of simultaneous increase of carrier mobility and decrease of carrier concentration at the doping of single crystal ε-MnSi with additional Mn atoms is not yet clear. A possible (but certainly open to discussions) reason qualitatively explaining experimental data has been proposed in Ref. 3. It presumes that: 1) the Mn doping induces the carrier localization on the defect center (e.g., the above discussed Si vacancy) in the MnSi matrix; 2) this doping also destroys collective (spin-polaron or Kondo type) resonance, probably existing in ε-MnSi single crystal.[24] The combination of these two effects obviously leads to the simultaneous decrease

of carrier concentration and the increase of carrier mobility, if we suggest that the additional carrier mobility decrease due to the carrier scattering on the defects is small compared to the carrier scattering on the collective resonance.

We are able to obtain additional information on the physical properties of the LT FM and HT FM phases analyzing the magneto-transport data for the SG film. If we present this film as two parallel conducting layers (see inset to the Fig. 7) the effective Hall resistivity can be written as

$$R_H = \frac{\rho_{H2}\sigma_2^2 d_2 + \rho_{H1}\sigma_1^2 d_1}{(\sigma_1 d_1 + \sigma_2 d_2)^2}, \tag{4}$$

where the indices "1" and "2" correspond to the lower (HT FM) and upper (LT FM) layer, respectively. From Eq. (4) it is seen that in thick films ($d \sim d_2 >> d_1$) the change of the Hall effect sign is possible when temperature decreases below upper layer Curie temperature ($T_{C2} \approx 46$ K) and the negative anomalous component of the Hall effect ($\rho^a_{H2} < 0$) in this layer starts to play a dominant role due to its similarity to the case of bulk ε-MnSi.[20,22]

The ratio between the conductivities of two layers σ_2/σ_1 can be roughly estimated using following assumptions: 1) the AHE resistivity of lower layer at $T < 200$ K is the same as for DG film,[3] i.e. $\rho^a_{H1} \approx +3.5{\cdot}10^{-6}$ Ω·cm; 2) the AHE resistivity of upper layer at $T = (25\text{-}40)$ K is the same as for ε-MnSi single crystal,[20,22] i.e. $\rho^a_{H2} \approx -(0.1\text{-}0.2){\cdot}10^{-6}$ Ω·cm; 3) the sign of the Hall effect changes to the opposite at the thickness $d = d_2 + d_1 = (70\text{-}90)$ nm (Figs. 7 and 8). Substituting these data in Eq.(4) we obtain the ratio $\sigma_2/\sigma_1 \sim 2$.

Let us verify this estimation using resistance value $R \approx 6.03$ and 2.15 Ω measured at 11.5K for samples 1 and 3 with different $d \approx 70$ and 160 nm, respectively. As the growth rates of Si-Mn films for these samples differ approximately twice, we first assume that conductivities of the layers 1 and 2 in these samples also differ. Using the "two-layer" model (see inset to the Fig. 7), we find:

$$\frac{R^{(1)}(11.5)}{R^{(3)}(11.5)} = \frac{1 + (\sigma_2^{(3)}/\sigma_1^{(3)})(d_2^{(3)}/d_1)}{1 + (\sigma_2^{(1)}/\sigma_1^{(1)})(d_2^{(1)}/d_1)}(\sigma_1^{(3)}/\sigma_1^{(1)}) \approx 2.8. \tag{5}$$

Here the top indexes refer to the sample number. Supposing that $\sigma_2^{(1)}/\sigma_1^{(1)} \approx 2$ and, $\sigma_1^{(3)}/\sigma_1^{(1)} \approx 1$, we find from Eq.(5) that: $\sigma_2^{(3)}/\sigma_1^{(3)} \approx 2.36$, i.e. close to the conductivity ratio above found from the Hall effect measurements.

Finally, we can estimate this ratio from the value of the resistance drop: $f(11.5\text{K}) = R(11.5\text{K})/R(290\text{K}) \approx 0.29$ and 0.21 for samples 1 and 3 with $d \approx 70$ and $d \approx 160$ nm, respectively. Let us pay attention to a similarity of the temperature dependences $R_{SG}(T)$ for SG grown samples with different thickness in the high temperature region $T \geq 220$ K (Fig. 9). This similarity means that at room temperature the conductivities of both layers are of the same order: $\sigma_2^{(3)} \approx \sigma_1^{(3)} \approx \sigma_2^{(1)} \approx \sigma_1^{(1)}$. Under these conditions,

$$\frac{f^{(1)}(11.5)}{f^{(3)}(11.5)} = \frac{1 + (\sigma_2^{(3)}/\sigma_1^{(3)})(d_2^{(3)}/d_1)}{1 + (\sigma_2^{(1)}/\sigma_1^{(1)})(d_2^{(1)}/d_1)}(\sigma_1^{(3)}/\sigma_1^{(1)})\frac{d_1 + d_2^{(1)}}{d_1 + d_2^{(3)}} \approx 1.38.$$

Putting here $\sigma_2^{(1)}/\sigma_1^{(1)} \approx 2$, we find $\sigma_2^{(3)}/\sigma_1^{(3)} \approx 2.67$, i.e. close to the estimation (5). So, the "two-layer" model works sufficiently well to describe magnetic and transport properties of SG grown Mn_xSi_{1-x} ($x \approx 0.52$) films.

Note one interesting conclusion following from above exposed consideration. In spite of a significant decrease of the nano-crystallites size in the interficial layer compared to that in the upper layer, the conductivity of bottom layer at low temperature does not significantly decrease. Probably, we observe here the effect of partial compensation of two effects (carrier concentration decrease and carrier mobility increase) having the same physical origin as in above discussed case of DG thin film.[3]

VI. CONCLUSIONS

In this work, we present the results of comparative study of magnetic and transport properties of nonstoichiometric Mn_xSi_{1-x} ($x \approx 0.51\text{-}0.52$) films grown in the non-conventional ("shadow")

geometry by the PLD method. We also compared them with the corresponding results for the films having an analogous chemical composition but grown in the conventional ("direct") geometry. The difference in physical properties of these two groups of films (SG or DG, respectively) is provided by the peculiarities of the used type of the PLD technology. The key point of SG approach is the using Kr as a scattering gas which results in the lower energy of deposited atoms. At the same time, the average deposition rate in the SG method is much higher than in the DG method.

X-ray diffraction analysis reveals that textured ε-MnSi-like phase with the B20-type crystal structure dominates in both SG and DG type of films. While the ε-MnSi single crystal has the Curie temperature $T_C \approx 30$ K,[8,9] the studied Mn_xSi_{1-x} films at $x \approx 0.52$ exhibit HT FM with $T_C > 300$ K accompanied by the manifestation of the positive sign of AHE. For SG grown Mn_xSi_{1-x} films, it is found that at low temperature the essential contribution to the magnetization is given by LT FM phase with $T_C \approx 46$ K; at the same time, AHE changes the sign from the positive to negative at $T \leq 30$K and film thickness $d \geq 90$ nm.

We explain these results as the manifestation of self-organizing effect in the SG polycrystalline Mn_xSi_{1-x} film, i.e. the formation of two layers with significantly different thickness and grain size, leading to the opposite sign contributions in to AHE. The bottom interface layer adjacent to $Al_2O_3(0001)$ substrate is ~ 10 nm in effective thickness with $T_C \approx 370$ K and consists of small (~ 5 nm) rounded grains. The top layer $\sim 60 - 260$ nm in thickness with a columnar grain structure ~ 50 nm in lateral size represents LT phase, which exhibits negative AHE similar to that in the ε-MnSi single crystal.[20,22]

We discuss the experimental results in terms of the model of defect-induced FM order with effective exchange coupling strongly affected by spin fluctuations[12] taking into account the structure peculiarities of studied films. We argue that the observed HT FM of nonstoichiometric Mn_xSi_{1-x} alloys strongly depends on the type of defects ("magnetically active" Si vacancies vs. "magnetically dead" interstitial Mn atom) as well as on the size of crystal grains which interfaces acting as the gettering regions for Si vacancies.

Nevertheless, the shape of grains can also play a crucial role in formation HT FM order (as in the case of dilute Si-Mn thin films[18]) as well as interface regions between grains. More investigations, including structural ones, are needed in order to understand the role of grains size, their shape and interface regions between them in formation HT FM order in SG grown films.

ACKNOWLEDGEMENTS

The work was partly supported by the RFBR (grant Nos. 14-07-91332, 14-07-00688, 14-47-03605, 14-22-01063, 15-29-01171, 13-07-12087, 13-07-00477), NBICS Center of the Kurchatov Institute and MIPT Center of Collective Usage with financial support from the Ministry of Education and Science of the Russian Federation (Grant No. RFMEFI59414X0009). The work at HZDR is financially supported by DFG (ZH 225/6-1). A.S.S. acknowledges the financial support of DAAD-MSU program "Vladimir Vernadsky".

[1] M. Hortamani, L. Sandratskii, P. Kratzer, I. Mertig, and M. Scheffler, Phys. Rev. B **78**, 104402 (2008).
[2] S. Kahwaji, R.A. Gordon, E.D. Crozier, and T.L. Monchesky, Phys. Rev. B **85**, 014405 (2012).
[3] V.V. Rylkov, S.N. Nikolaev, K.Yu. Chernoglazov, B.A. Aronzon, K.I. Maslakov, V.V. Tugushev, E.T. Kulatov, I.A. Likhachev, E.M. Pashaev, A.S. Semisalova, N.S. Perov, A.B. Granovskii, E.A. Gan'shina, O.A. Novodvorskii, O.D. Khramova, E.V. Khaidukov, and V.Ya. Panchenko, JETP Lett. **96**, 255 (2012).
[4] V.V. Rylkov, E.A. Gan'shina, O.A. Novodvorskii, S.N. Nikolaev, A.I. Novikov, E.T. Kulatov, V.V. Tugushev, A.B. Granovskii, and V.Ya. Panchenko, Europhys. Lett. **103**, 57014 (2013).
[5] Y. Li, N. Kanazawa, X.Z. Yu, A. Tsukazaki, M. Kawasaki, M. Ichikawa, X.F. Jin, F. Kagawa, and Y. Tokura, Phys. Rev. Lett. **110**, 117202 (2013); T.L. Monchesky, J.C. Loudon, M.D. Robertson, and A.N. Bogdanov, *ibid.* **112**, 059701 (2014).
[6] S.A. Meynell, M.N. Wilson, J.C. Loudon, A. Spitzig, F.N. Rybakov, M.B. Johnson, and T.L. Monchesky, Phys. Rev. B **90**, 224419 (2014).
[7] A. Yang, K. Zhang, S. Yan, S. Kang, Y. Qin, J. Pei, L. He, H. Li, Y. Dai, S. Xiao, and Y. Tian, J. Alloys Comp. **623**, 438 (2015).
[8] T. Moriya, *Fluctuations in Itinerant ElectronMagnetism* (Springer-Verlag, Berlin, 1985).
[9] S.M. Stishov and A.E. Petrova, Phys. Usp. **54**, 1117 (2011).
[10] A.E. Petrova, V.N. Krasnorussky, A.A. Shikov, W.M. Yuhasz, T.A. Lograsso, J.C. Lashley, and S.M. Stishov, Phys. Rev. B **82**, 155124 (2010).

[11] S. Kahwaji, R.A. Gordon, E.D. Crozier, S. Roorda, M.D. Robertson, J. Zhu, and T.L. Monchesky, Phys. Rev. B **88**, 174419 (2013).
[12] V.N. Men'shov, V.V. Tugushev, S. Caprara, and E.V. Chulkov, Phys. Rev. B **83**, 035201 (2011).
[13] V.V. Rylkov, A.S. Bugaev, O.A. Novodvorskii, V.V. Tugushev, E.T. Kulatov, A.V. Zenkevich, A.S. Semisalova, S.N. Nikolaev, A.S. Vedeneev, A.V. Shorokhov, D.V. Aver'yanov, K.Yu. Chernoglazov, E.A. Gan'shina, A.B. Granovsky, Y. Wang, V.Ya. Panchenko, and S. Zhou, J. Magn. Magn. Mater. **383**, 39 (2015).
[14] V.V. Rylkov, B.A. Aronzon, A.S. Lagutin, V.V. Podol'skii, V.P. Lesnikov, M. Goiran, J. Galibert, B. Raquet, and J. Léotin, J. Exp. Theor. Phys. **108**, 149 (2009).
[15] B.A. Aronzon, A.B. Granovskii, S.N. Nikolaev, D.Yu. Kovalev, N.S. Perov, and V.V. Rylkov, Phys. Solid State **46**, 1482 (2004).
[16] M. Walterfang, W. Keune, K. Trounov, and R. Peters, Phys. Rev. B **73**, 214423 (2006).
[17] Y.T. Zhang, Q. Jiang, D.J. Smith, and J. Drucker, J. Appl. Phys. **98**, 033512 (2005).
[18] S. Kahwaji, W. Bowman, M.D. Robertson, and T.L. Monchesky, J. Appl. Phys. **113**, 063910 (2013).
[19] M. Jamet, A. Barski, T. Devillers, V. Poydenot, R. Dujardin, P. Bayle-Guillemaud, J. Rothman, E. Bellet-Amalric, A. Marty, J. Cibert, R. Mattana, and S. Tatarenko, Nature Mater. **5**, 653 (2006).
[20] M. Lee, Y. Onose, Y. Tokura, and N.P. Ong, Phys. Rev. B **75**, 172403 (2007).
[21] N. Nagaosa, J. Sinova, S. Onoda, A.H. MacDonald, and N.P. Ong, Rev. Mod. Phys. **82**, 1539 (2010).
[22] M. Lee, W. Kang, Y. Onose, Y. Tokura, and N.P. Ong, Phys. Rev. Lett. **102**, 186601 (2009); A. Neubauer, C. Pfleiderer, B. Binz, A. Rosch, R. Ritz, P.G. Niklowitz, and P. Boni, *ibid.* **102**, 186602 (2009).
[23] Jia-Hsien Yao, Hsiu-Hau Lin, Yun-Liang Soo, Tai-Sing Wu, Jai-Lin Tsai, Ming-Der Lan, and Tsung-Shune Chin, Appl. Phys. Lett. **100**, 092404 (2012).
[24] S.V. Demishev, V.V. Glushkov, I.I. Lobanova, M.A. Anisimov, V.Yu. Ivanov, T.V. Ishchenko, M.S. Karasev, N.A. Samarin, N.E. Sluchanko, V.M. Zimin, and A. V. Semeno, Phys. Rev. B **85**, 045131 (2012); S.V. Demishev, A.V. Semeno, A.V. Bogach, V.V. Glushkov, N.E. Sluchanko, N.A. Samarin, and A.L. Chernobrovkin, JETP Lett. **93**, 213 (2011).
[25] S. Okada, T. Shishido, Y. Ishizawa, M. Ogawa, K. Kudou, T. Fukuda, and T. Lundstrom, J. Alloys Comp. **317–318**, 315 (2001).